Ultramicroscopy 162 (2016) 52–60

Contents lists available at ScienceDirect

Ultramicroscopy

journal homepage: www.elsevier.com/locate/ultramic

Full length article

Oxidation-state sensitive imaging of cerium dioxide by atomic-resolution low-angle annular dark field scanning transmission electron microscopy

Aaron C. Johnston-Peck [a,*], Jonathan P. Winterstein [b], Alan D. Roberts [c], Joseph S. DuChene [c], Kun Qian [c], Brendan C. Sweeny [c], Wei David Wei [c], Renu Sharma [b], Eric A. Stach [d], Andrew A. Herzing [a]

[a] Materials Measurement Lab, National Institute of Standards Technology, Gaithersburg, MD 20899, USA
[b] Center for Nanoscale Science and Technology, National Institute of Standards Technology, Gaithersburg, MD 20899, USA
[c] Department of Chemistry and Center for Nanostructured Electronic Materials, University of Florida, Gainesville, FL 32611, USA
[d] Center for Functional Nanomaterials, Brookhaven National Laboratory, Upton, NY 11793, USA

ARTICLE INFO

Article history:
Received 25 August 2015
Received in revised form
8 December 2015
Accepted 15 December 2015
Available online 17 December 2015

Keywords:
Scanning transmission electron microscopy
Point defects
Cerium dioxide

ABSTRACT

Low-angle annular dark field (LAADF) scanning transmission electron microscopy (STEM) imaging is presented as a method that is sensitive to the oxidation state of cerium ions in CeO_2 nanoparticles. This relationship was validated through electron energy loss spectroscopy (EELS), *in situ* measurements, as well as multislice image simulations. Static displacements caused by the increased ionic radius of Ce^{3+} influence the electron channeling process and increase electron scattering to low angles while reducing scatter to high angles. This process manifests itself by reducing the high-angle annular dark field (HAADF) signal intensity while increasing the LAADF signal intensity in close proximity to Ce^{3+} ions. This technique can supplement STEM-EELS and in so doing, relax the experimental challenges associated with acquiring oxidation state information at high spatial resolutions.

Published by Elsevier B.V.

1. Introduction

Cerium dioxide (CeO_2, ceria) is a rare-earth oxide which exhibits a fluorite-type structure where the cerium ion has formal charge of 4^+ and is coordinated to 8 oxygen ions with a formal charge of 2^-. In a reducing environment, oxygen vacancies are formed and electrons become localized at the cerium ions. As a result, their formal charge becomes 3^+ and the electronic structure is correspondingly altered. A considerable amount of research has been conducted to develop an understanding of the reduction and oxidation behavior of ceria [1]. X-ray absorption spectroscopy (XAS) and X-ray photoelectron spectroscopy (XPS) are useful in characterizing ceria because they are sensitive to bonding environment. However, XAS and XPS lack high spatial resolution and struggle to deduce localized changes in behavior due to features such as defects, interfaces, or coordination number. Scanning transmission electron microscopy (STEM) when coupled with electron energy loss spectroscopy (EELS) can collect signals containing similar information with significantly better spatial resolution than X-ray techniques. EELS has been regularly used to qualitatively, as well as quantitatively, track changes in the oxidation state of cerium by monitoring changes in the Ce $M_{4,5}$ edge [2,3]. Impressively, STEM-EELS has successfully tracked changes in composition and bonding environment in a variety of materials at atomic-scale spatial resolution [4–7], including ceria nanoparticles [8].

The study by Turner et al. [8] highlights the power of atomically-resolved EELS by identifying facet- and defect-dependent behavior at the surface of ceria nanoparticles. While EELS measurements acquired with atomic spatial resolution in the scanning transmission electron microscope have become increasingly common, they impose exacting experimental and instrumental requirements. Achieving a sufficient signal above both noise and background to discern bonding information requires a large electron dose while maintaining the required spatial and energy resolution. Therefore, aberration-correcting optics are critical to increase the numerical aperture and thus probe current without increasing the probe size [6]. Furthermore, corrective optics are also necessary in the EEL spectrometer so that a large collection angle can be employed without sacrificing energy resolution [9,10]. The need for a large collection angle arises from the need to improve signal collection efficiency as well as to reduce artifacts due to elastic scattering [11,12]. Maintaining sufficient energy resolution also suggests that a cold field emission gun (CFEG) or monochromated source is preferable such that feature broadening

* Corresponding author.
E-mail address: aaron.johnston-peck@nist.gov (A.C. Johnston-Peck).

http://dx.doi.org/10.1016/j.ultramic.2015.12.004
0304-3991/Published by Elsevier B.V.

in the spectra is dominated by intrinsic material properties, such as core–hole lifetimes, rather than the initial energy spread of the incident electrons [13,14]. In addition to specialized equipment, the microscope must be housed in a highly stable environment to ensure that instability of the sample and optical components are minimized [15]. Lastly, beam damage is a consistent concern for any electron-dose-heavy experiments. Specific to CeO_2, previous studies have demonstrated that the electron beam acts in a reducing manner and drives the transition from Ce^{4+} to Ce^{3+} as reflected in EELS and high-resolution transmission electron microscopy (HRTEM) exit wave reconstruction measurements [16–18]. It is worth noting that this effect is not limited to electron-based techniques, as any high energy radiation, such as X-rays, can also reduce CeO_2 [19–21]. Therefore, the use of lower accelerating voltages and short probe dwell times to minimize beam damage further emphasizes the importance of efficient experimental design and aberration-correcting optics [7,22].

This demanding experimental protocol limits the number of suitable microscopes that are able to execute these experiments. Moreover, it significantly reduces the possibility that these types of measurements will be successfully executed under *in situ* conditions of flowing gases or elevated temperatures where sample drift is typically greater. Given all these considerations, it seems prudent when possible that other techniques with less demanding experimental requirements be used to supplement or replace EELS measurements. Imaging based techniques relax equipment requirements while retaining the ability to acquire data with atomic spatial resolution. Moreover, the acquisition of images requires less electron dose than EELS spectrum images, thus lessening the possibility of beam induced artifacts.

In this report, we present an alternative to STEM-EELS based on low-angle annular dark field (LAADF) STEM imaging as a proxy for changes in the oxidation state of cerium ions in nanoscale particles. Annular dark field images are dominated by elastic and thermal diffuse scattering (TDS). The relative proportion of these two will vary as a function of collection angle because elastic scattering dominates at lower angles while TDS dominates at higher angles [23]. As a result, the contrast mechanisms of LAADF and high-angle annular dark field (HAADF) imaging are different. HAADF imaging is more sensitive to changes in atomic number while LAADF imaging is more sensitive to variations in structure (i.e., diffraction conditions). Accordingly, LAADF has been successfully used to visualize strain fields [24–27], line or planar defects [28,29], as well as, in one case, oxygen vacancies in a $SrTiO_3$ thin film [30]. Utilizing an imaging technique rather than a spectroscopic approach we are able to qualitatively identify changes in the oxidation state of ceria nanoparticles with high spatial resolution. This imaging approach requires less specialized equipment than previous high spatial resolution STEM-EELS studies on ceria [8]. Additionally, it offers the added benefit of a lower overall electron dose requirement. Furthermore, preliminary experiments on MgO and $SrTiO_3$ suggest that other nanoscale materials are suitable for this technique.

2. Materials and methods

2.1. Particle synthesis

CeO_2 octahedra were prepared according to a protocol previously described by Wu et al. [31]. Two separate solutions (A and B) were first prepared and then combined together to reach a total reaction solution volume of 40 mL. Solution A is composed of 0.434 g cerium nitrate ($Ce(NO_3)_3$) in 30 mL Nanopure H_2O and Solution B is composed of 0.0038 g sodium phosphate (Na_3PO_4) in 10 mL Nanopure H_2O. Solutions A and B were then combined and sonicated for 10 min. The 40 mL solution was then transferred to a Teflon-lined autoclave, sealed and heated at 170 °C for 8 h to produce octahedral nanostructures. After the given reaction time had elapsed, the samples were removed from the oven and allowed to cool to ambient temperature. CeO_2 octahedra were then washed with Nanopure H_2O and centrifuged three times at 837.8 rad/s for 5 min and finally dried in an oven at 60 °C overnight to obtain a dry CeO_2 powder.

CeO_2 cubes were synthesized according to a previous literature report [32]. Briefly, 9.60 g sodium hydroxide (NaOH) and 0.868 g of $Ce(NO_3)_3$ was dissolved in 50 mL Nanopure H_2O. The solution was sonicated for 10 min and then transferred to a Teflon-lined autoclave, sealed and heated at 180 °C for 24 h. After the reaction, samples were removed from the oven and allowed to cool to ambient temperature. CeO_2 cubes were then washed with Nanopure H_2O and centrifuged three times at 837.8 rad/s for 5 min and finally dried in an oven at 60 °C overnight to obtain a dry CeO_2 powder.

$SrTiO_3$ cubes were prepared following a method described previously by Rabuffetti and co-workers [33]. Briefly, 1.945 g of strontium hydroxide ($Sr(OH)_2$) was dispersed in 40 mL of a 1 mol/dm^3 acetic acid solution, while a separate solution of 2.483 mL titanium butoxide ($Ti(OCH_2CH_2CH_2CH_3)_4$) was mixed thoroughly in 2.432 mL of 12 mol/dm^3 hydrochloric acid (HCl) and 11 mL ethanol. Once thoroughly mixed, the solution of titanium butoxide in HCl/ethanol was added slowly to the solution of strontium hydroxide and acetic acid. Precipitation of the $SrTiO_3$ was induced by the addition of 5 g NaOH and the suspension was allowed to stir for 10 min. Following stirring, the solution was loaded into a Teflon-lined autoclave and heated at 240 °C for 24 h. After cooling to room temperature, the precipitate was centrifuged twice at 1047.2 rad/s for 5 min, the precipitate was collected and dried overnight at 60 °C to obtain the $SrTiO_3$ powder.

MgO cubes were synthesized by combustion of Mg ribbon in a fume hood, resulting in a plume of cube-shaped MgO particles [34]. A holey carbon film supported on a copper TEM grid was held in the plume allowing the particles to be directly deposited onto the carbon film. The sample was prepared months before the data in this report was collected .

2.2. Microscopy

Images and EELS data were acquired on an aberration corrected FEI Titan 80–300 operated at 300 kV and a Hitachi HD-2700C operated at 120 kV and 200 kV. The probe convergence semi-angles (α) used were 14 mrad (Titan 80–300) and 21 mrad (HD-2700C). The inner collection angles (θ_{inner}) of the annular dark field (ADF) detectors were determined by directly mapping the response of the detector rather than using the shadow of the detector which can underestimate the inner angle [35]. The data in Figs. 1, 2, 6, 7, and Supporting Information 1 and 2 were collected on the FEI Titan 80–300 while the data in Fig. 3 and 8 were collected on the Hitachi HD-2700C. The outer collection angle (θ_{outer}) was calculated using a geometric relation based on the detector response map and measured inner angle. Table 1 outlines the collection angles of the FEI Titan 80–300. Images acquired at camera lengths (CLs) of 300, 245, and 195 mm would be considered as LAADF and images acquired at CLs of 100, 77, and 60 mm could be considered as HAADF. The remaining CLs, 160 mm and 130 mm, fall under an intermediary designation of MAADF (medium-angle annular dark field). In the literature, there is some variation in the definition of what ranges of collection angles precisely qualify as HAADF or LAADF imaging [36–38]. While the designations made here may not precisely conform to all the definitions in the literature they capture the general trend of transitioning from an image with a large

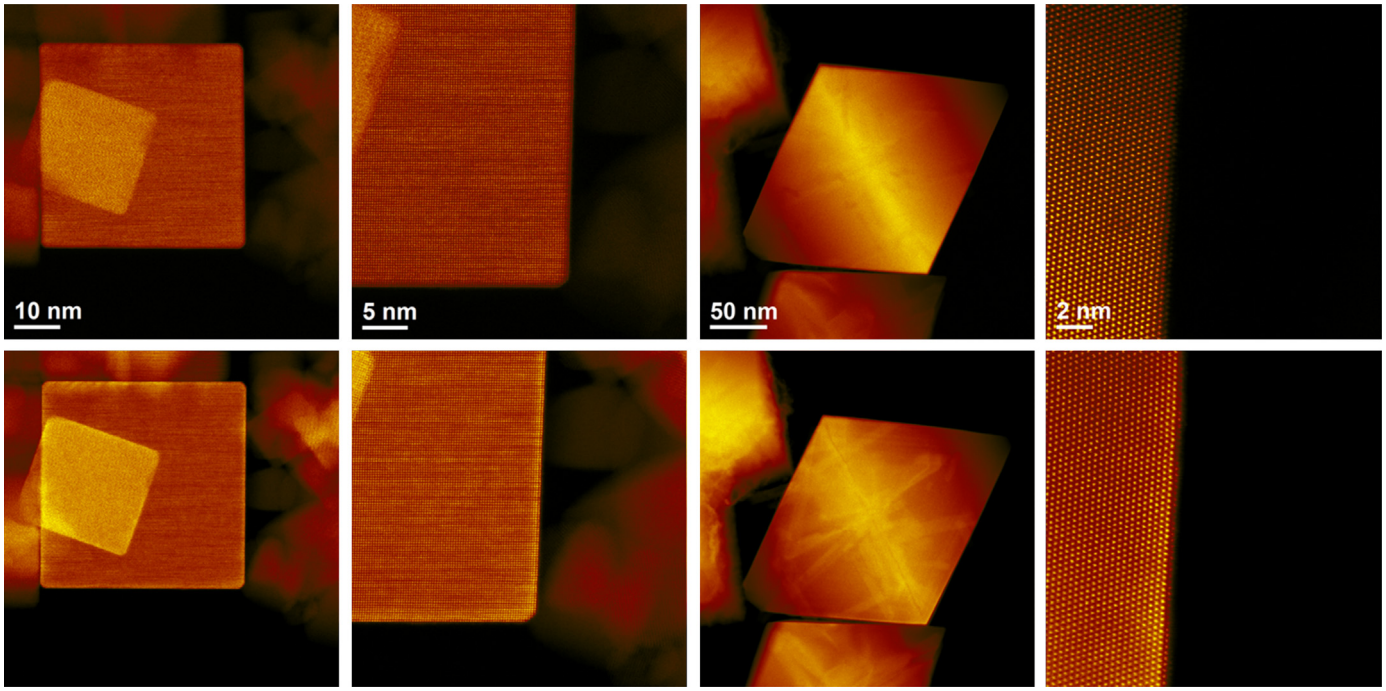

Fig. 1. (top row) HAADF and (bottom row) LAADF STEM images of a cube and truncated octahedron CeO_2 particles. LAADF and HAADF images were acquired with a camera length of 300 mm and 77 mm respectively.
Note: The scan rotation of the high magnification images was changed relative to the low magnification images of the truncated octahedron CeO_2 nanoparticle.

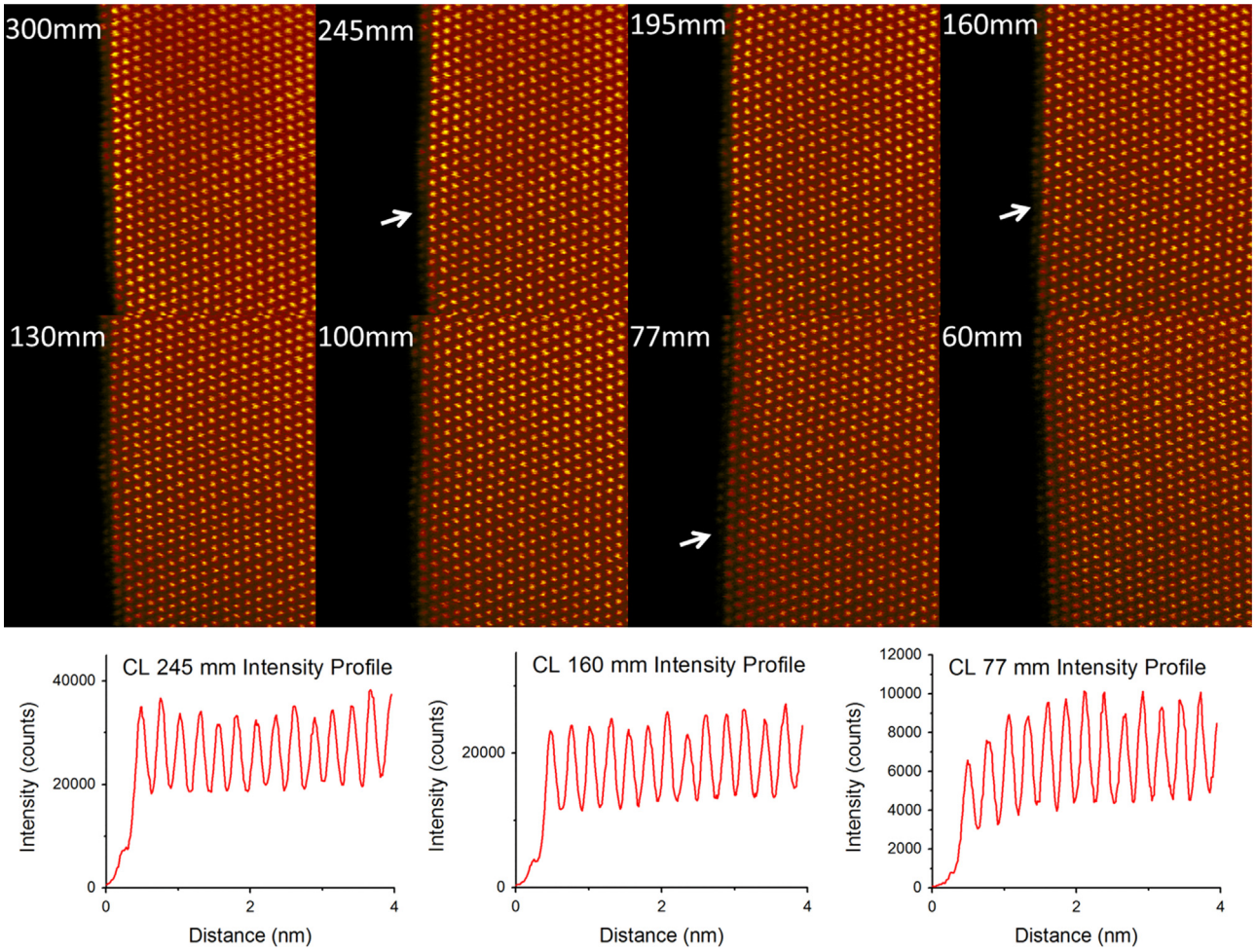

Fig. 2. A series of ADF images acquired from a truncated octahedron particle over a range of camera lengths, the inner collection angle on the detector decreases as the camera length is shorted. The arrow indicates the location of where select line profiles are shown of camera lengths 245, 160, and 77 mm.

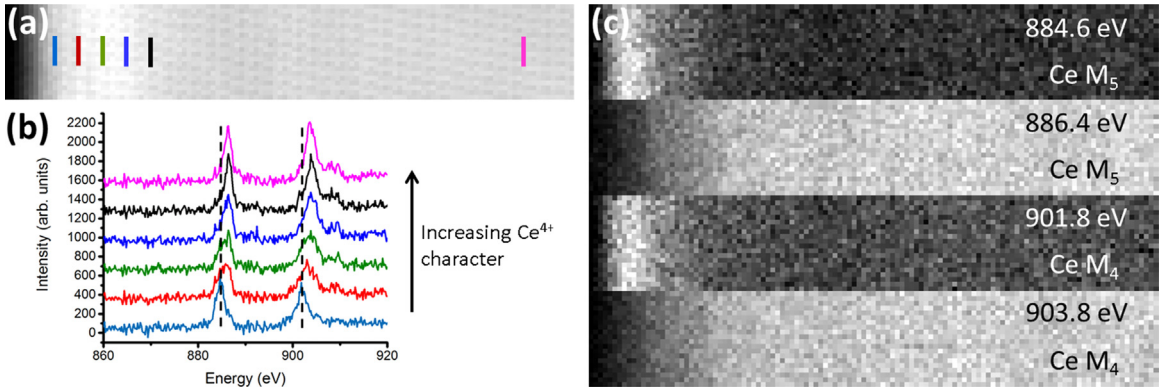

Fig. 3. STEM EELS spectrum image along a (100) surface of a ceria cube. Averaged (1 × 6) spectra (b) of the Ce $M_{4,5}$ edge from different positions, as specified on the LAADF STEM image (a), indicating different oxidation states. Also shown are 1 eV wide slices (c) extracted from the spectrum image with the central energy value indicated. (For interpretation of the references to color in this figure legend, the reader is referred to the web version of this article.)

component of electrons that have been coherently scattered (LAADF) or incoherently scattered (HAADF).

In situ studies were conducted on a FEI Titan environmental scanning transmission electron microscope (ESTEM) operated at 300 kV with a probe convergence semi angle of 10 mrad. The inner collection angle was 35 mrad, which was also determined by directly mapping the response of the detector. The high-angle scatter is subtended by a differential pumping aperture which limits the outer scattering angle to 75 mrad. The data shown in Fig. 4 was collected on the FEI Titan ESTEM.

It should be noted that the central transmitted spot in the diffraction pattern must be accurately centered inside of the annular detector. This is especially important at camera lengths where the convergence angle is similar to the inner collection angle, as misalignment can cause the transmitted beam to impinge on the active portion of the detector. Also, the incident probe when scanned over a large area (e.g. at low magnifications) can cause a significant shift of the direct beam with respect to the detector. In this case, a de-scan routine was implemented to ensure the direct beam remains stationary and does not overlap with the detector. If such care is not taken and the direct beam overlaps the detector, the contrast mechanisms are altered significantly in comparison with the LAADF imaging mode. In this configuration, fringes are observed at the perimeter of the particle, which are not reflective of the local oxidation state, as different physical phenomena are responsible for the collected electron signal. Additional details can be found in the Supporting Information.

3. Results and discussion

Annular dark field images of typical ceria nanoparticles are shown in Fig. 1. Two types of ceria samples were used in this study: cubes and truncated octahedra. The cubes are predominately terminated by {100} surfaces while the truncated octahedra are predominately terminated by {100} and {111} surfaces.

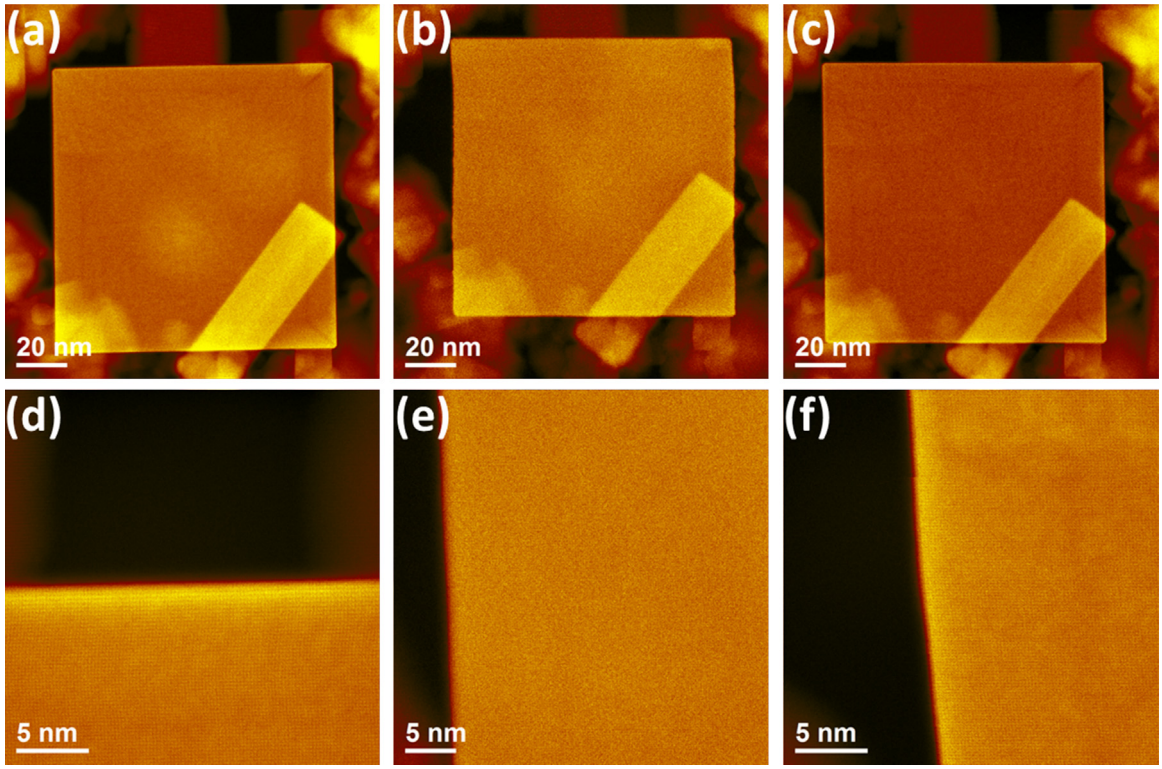

Fig. 4. LAADF STEM images of a ceria cube under different gas environments: (a, d) 25 °C, vacuum (b, e) 300 °C, 0.5 mbar oxygen (c, f) 25 °C, 0.1 mbar hydrogen.

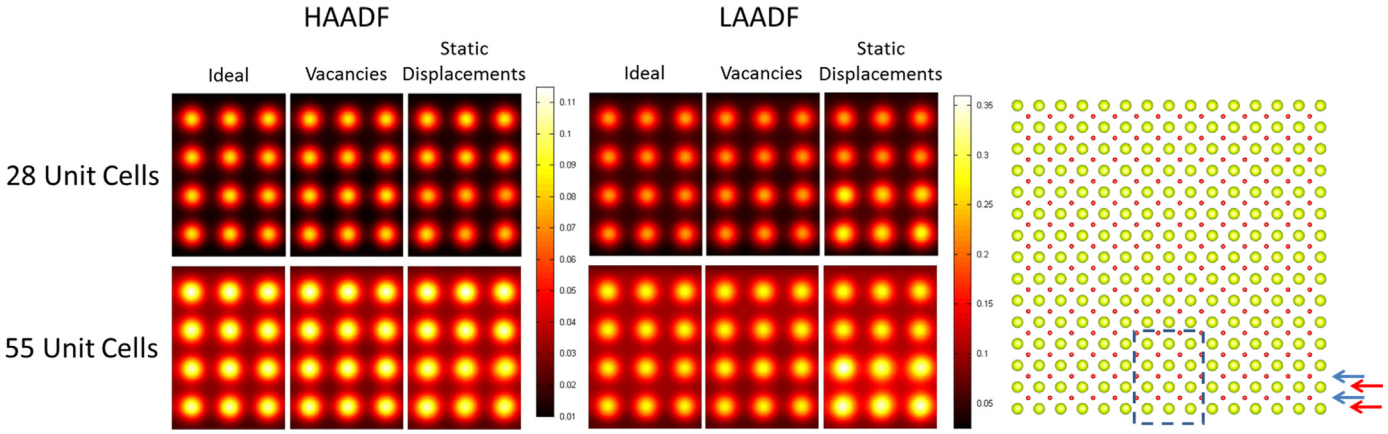

Fig. 5. Multislice simulated LAADF and HAADF STEM images of $<100>$ orientated CeO_2 using an ideal model, one with oxygen vacancies, and one with random static displacements of the Ce atoms. The model depicts the supercell used in the simulations with the blue dashed box outlining the subregion used for simulations. The blue and red arrows indicate the atomic rows where the oxygen vacancies and displacements were introduced, respectively. (For interpretation of the references to color in this figure legend, the reader is referred to the web version of this article.)

The images on the top row were acquired under HAADF conditions while the images on the bottom row are taken under LAADF conditions. Differences between the HAADF and LAADF images are apparent, specifically, the image intensity increases in the LAADF images at the edges of the particles creating a bright band at the periphery. This increased intensity at the surface was always observed in the LAADF images whenever the particle was oriented along a high symmetry zone axis; a condition which supports strong channeling of the electron beam onto the atomic columns. In contrast, no such difference between the HAADF and LAADF images were observed when the particle was tilted away from a high symmetry condition (see Supporting Information Fig. S2). To better understand this phenomenon, a series of images was acquired using a range of camera lengths, which changes the collection angles of the detector, and thus the type of scattering mechanism which predominately contributes to the signal. Fig. 2 presents a series of images acquired from a truncated octahedron particle oriented along a $<110>$ zone axis such that the {111} facet was viewed edge-on. At long camera lengths (e.g., 245 mm, LAADF), the particle shows a bright ring around the perimeter. A line profile originating at the particle edge reveals that the intensity in the first two atomic columns, ignoring the first and

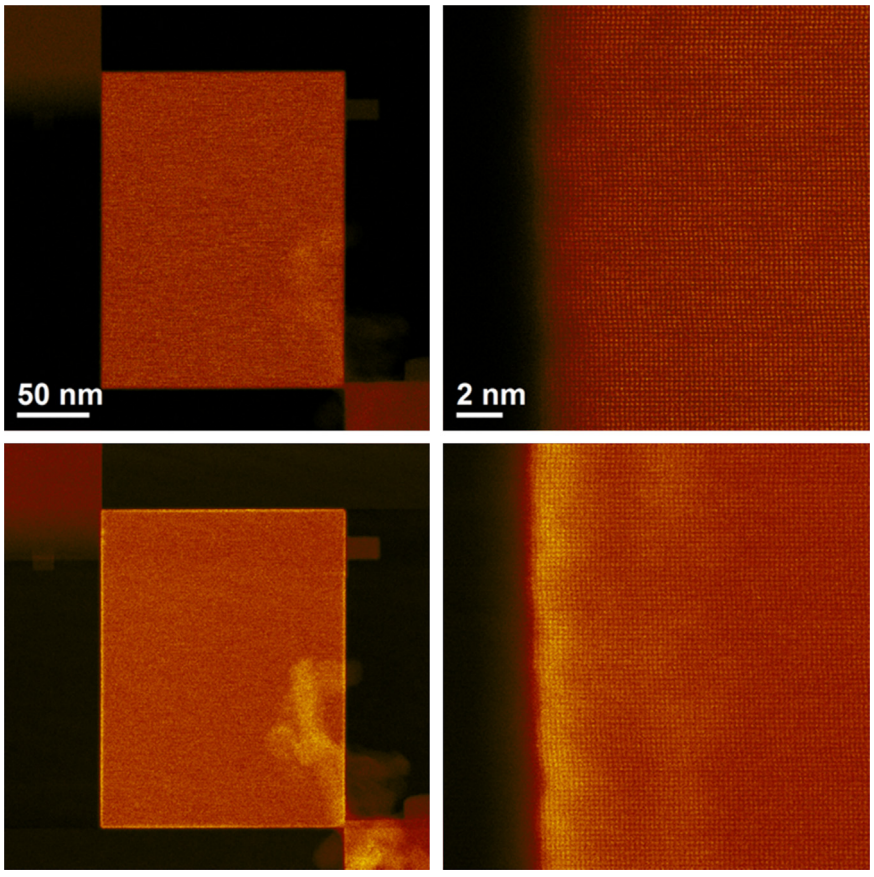

Fig. 6. HAADF (top row) and LAADF STEM (bottom row) images of a MgO smoke cube showing an increase in scattering to low angles at the edges of the particle accompanied by a reduction in HAADF signal intensity at the edges.

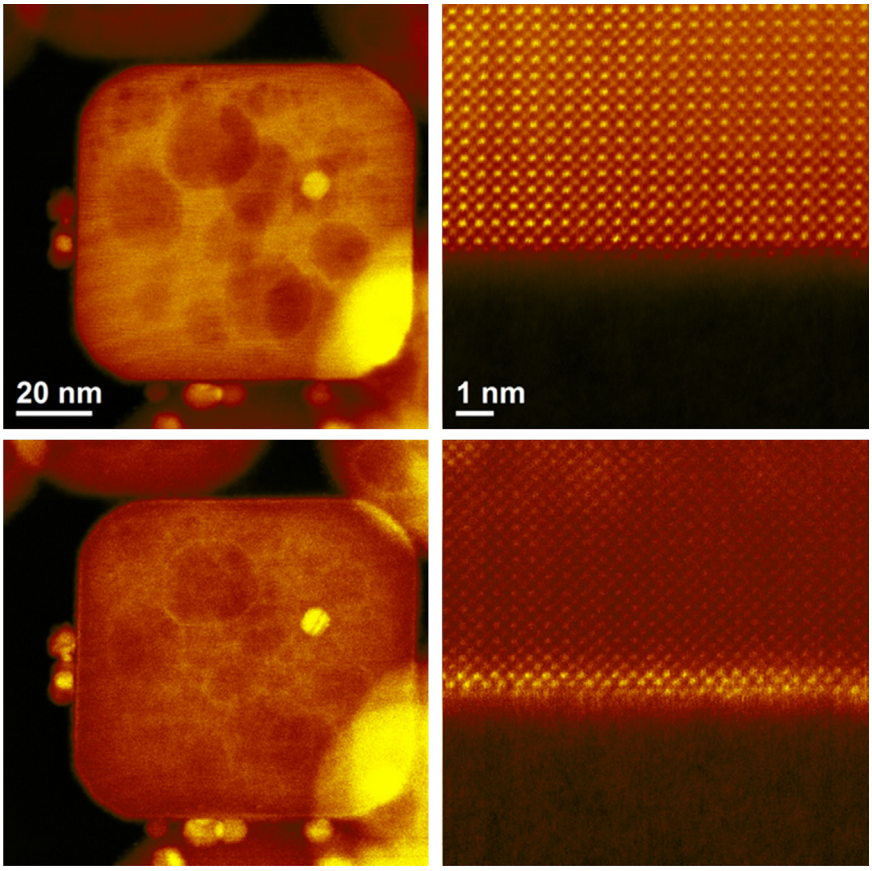

Fig. 7. MAADF (top row) and LAADF STEM (bottom row) images of $SrTiO_3$ cubes supporting Au nanoparticles showing an increase in scattering to low angles at the edges of the cube.

Table 1
FEI Titan 80–300 ADF collection angles as a function of camera length.

CL (mm)	θ_{inner} (mrad)	θ_{outer} (mrad)
300	23	129
245	28	159
195	35	195
160	42	240
130	58	326
100	71	400
77	88	498
60	112	635

incomplete atomic column at the outermost edge, is greater than that of the immediately adjacent columns in the line profile. As the camera length is shortened (e.g., 160 mm, MAADF) the line profile reveals a relatively uniform intensity. As the camera length is further shortened (e.g., 77 mm, HAADF) the intensity in the atomic columns at the particle edge becomes less than those in the adjacent columns. The line profile from this image reveals a decrease in intensity in the first two complete atomic columns. This shows that the edges of the particles scatter more strongly to lower angles than the rest of the particle while the columns further from the surface scatter more strongly to higher angles. Therefore, the uniform intensity under MAADF conditions represents a balance between the low- and high-angle scattering.

Previous studies using STEM-EELS have indicated that the surface layers of ceria are reduced [8,18,19]. Additionally a study by Lin et al. [39] comparing HRTEM images to multislice image simulations concluded that the surfaces of ceria particles contain oxygen vacancies. If present here, it is likely that these point defects are influencing the image contrast, similar to the behavior reported by Muller et al. [30]. To establish a link between reduced ceria and contrast changes in LAADF and HAADF image signals, like those observed in Fig. 1 and 2, a combination of tools were used to identify and understand the origin of the observed behavior. EELS was used to confirm the presence of reduced cerium ions at the surface. *In situ* experiments further demonstrated that the presence of oxygen vacancies (reduced ceria) and the observed contrast are intimately linked. Finally, multislice image simulations aided the interpretation of the physical origin of the changes in electron scattering that lead to the observed image contrast.

First, EELS was used to compare the measured oxidation state with LAADF image intensity for ceria nanocubes. The electron loss near edge structure (ELNES) of the Ce $M_{4,5}$ edges can be used to determine the cerium oxidation state and has been well documented in the CeO_2 system [2,8]. Spectra were collected along a {100} facet of a cube oriented along the $<100>$ zone axis. A spectrum image was acquired at 120 kV by scanning in (0.0982×0.0982) nm steps over an area of (1.964×11.685) nm. The EELS signal was integrated for 200 ms to minimize beam damage and the LAADF signal (Fig. 3a) was acquired in parallel. As before, an increase in the LAADF signal is apparent at the edge of the particle (Fig. 3a). EELS spectra, showing the structure and position of the Ce $M_{4,5}$ edge, were extracted from the spectrum image and averaged $(1 \times 6$ pixels) from several key points along the particle (indicated by colored lines in the image). The dark blue line in the LAADF image demarcates the approximate boundary where the signal in the LAADF images begins to increase near the particle edge. In the region near the particle edge, the ELNES features (Fig. 3b) gradually change as a function of position moving from the particle edge towards the boundary, i.e., from the

light blue spectra to the dark blue spectra. The peaks in the extracted spectrum in this region exhibit both a shift to higher energies as well as a change in peak shape moving away from the edge of the particle. This transition is characteristic of an evolution from a predominantly Ce^{3+} state to that of a predominately Ce^{4+} state. The black spectrum lies just outside the brighter region of the LAADF image and, in comparison to the light blue spectrum from the particle edge, has shifted considerably in energy. By comparison, the shape and energy of the Ce $M_{4,5}$ edge in the inner region remain relatively static as a function of position, which is apparent when comparing the black and purple spectra. Therefore, this contrast change in the LAADF images corresponds to a transition in oxidation state, which indicates that the change in contrast is sensitive to the oxidation state of the cerium (i.e. the presence of oxygen vacancies).

The change in LAADF image intensity and spectrum image information (ELNES) is well correlated, such that the increased LAADF signal is observed only in areas where Ce^{3+} character is observed. As CeO_2 is reduced to CeO_{2-x} the lattice parameter increases, a phenomenon sometimes referred to as chemical expansion [40,41]. This occurs because the ionic radius of Ce^{3+} (0.114 nm) is larger than Ce^{4+} (0.097 nm) [42]. Locally, in the presence of a vacancy it is expected that the Ce ions relax outward from the vacancy site while O ions will contract [43]. This process distorts the lattice but the correlation between the LAADF image intensity and spectrum image information indicates that the strain fields resulting from the reduction decay over distances on the order of a single unit cell or less. Therefore, the LAADF signal provides a spatially accurate proxy for the location of reduced cerium ions in the particle, since the increased low-angle scattering is localized around these reduced ions. This high degree of localization will enable studying the differences between specific facets or the behavior around defects such as surface steps and pores.

LAADF-STEM imaging was also carried out *in situ* using an FEI Titan ESTEM system in an effort to corroborate the EELS data. A ceria cube was imaged along the [001] zone axis. Under high vacuum and room temperature, conditions similar to those used to acquire the data in Figs. 1 and 2, the bright ring around the particle perimeter was again observed in LAADF imaging (Fig. 4a and d). Complimentary HAADF imaging in the ETEM is impossible due to the differential pumping apertures which limit the scattering angles to 75 mrad. When subjected to oxidizing conditions ($\approx$ 50 Pa O_2, 300 °C) the contrast at the particle periphery was diminished (Fig. 4b and e). Upon return to conditions that were more amenable to oxygen vacancy formation ($\approx$ 10 Pa H_2, room temperature) increased scattering to low angles at the particle edge was observed again (Fig. 4c and f). The correlation of the degree of small angle scattering with the oxidation potential of the environment further substantiates that the presence of oxygen vacancies and therefore Ce^{3+} are responsible for the observed variation in signal intensity.

It is clear that the presence of reduced ceria is responsible for the variations in signal intensity seen at the edges of the particle. Multislice image simulations were used to further understand the physical mechanism behind the increased scattering to low angles produced by surface reduction. These simulations were carried out by constructing a $7\times7\times55$ supercell based on the CeO_2 cubic unit cell (a=0.5411 nm) and oriented along the [001] zone axis using QSTEM [44]. A rectangular region that terminated along a $<100>$ facet was sampled, the edges of the supercell were padded to prevent artifacts that may result from sampling a non-periodic structure. The simulation parameters used were chosen to approximate the imaging conditions on the FEI Titan 80–300, details can be found in the Supporting Information. A total of 16 phonon configurations were calculated, and B factors of 0.00509 nm^2 and 0.00761 nm^2 were used for the cerium and oxygen atoms, respectively [45]. Simulations from the structure were calculated at two different thicknesses (28 unit cells or $\approx$ 15 nm and 55 unit cells or $\approx$ 30 nm) and two different ranges of collection angle corresponding to LAADF and HAADF imaging conditions (28 mrad to 159 mrad and 88 mrad to 215 mrad, respectively). When an ideal structure with no defects or distortions is used, the intensity in both the LAADF and HAADF images is consistent and does not show variation as a function of position. To account for the effect of oxygen vacancies, which both EELS and ETEM indicated were present, oxygen vacancies were randomly introduced to the first two atomic layers of oxygen in the model. In order to represent a complete transition to the Ce^{3+} state, the lattice sites of the oxygen were defined to have a site occupancy of 50%. In the multislice results from the defective structures shown in the middle column of Fig. 5, the HAADF and LAADF images have nearly identical intensity in regions with and without the oxygen vacancies. This indicates that a lack of oxygen atoms is not solely responsible for the contrast observed in the experimental images. Instead, the increased low-angle scattering observed in the reduced regions of the specimen is more likely due to lattice distortion caused by removal of the oxygen.

As previously discussed, the lattice of CeO_2 distorts as it is reduced to CeO_{2-x}, a process related to the increased ionic radius of Ce^{3+} relative to Ce^{4+} [42]. To represent this distortion in the supercell, all of the cerium atom positions in the first two atomic layers were randomly displaced according to a Gaussian distribution with a deviation of 0.010822 nm, or 2% of the lattice parameter. It is unlikely that this approach is a completely accurate physical representation of the distortion caused by the oxygen vacancies and increase in the ionic radii of the cerium ions in ceria because the displacement of the atoms is not correlated, and the magnitude of the displacement may not be accurate. However, it should be sufficient to give a first approximation of the structure by generating what is equivalent to a random strain field [26]. In this case, the multislice results (Fig. 5, rightmost column) show that the lattice distortion is accompanied by a drop in intensity of the HAADF image and an increase in the intensity of the LAADF image. This indicates that the change in intensity is due to the reorganization and distortion of the lattice that occurs when ceria is reduced. Additional simulations were run using supercells where only a fraction of cerium atoms in the first two atomic layers were displaced, leaving some cerium atoms at their native positions. As the portion of displaced cerium atoms decreases, the relative changes in the LAADF and HAADF signals relative to the perfect portion of the supercell also decreases (Supporting Information Fig. S3). This further indicates that static displacements are responsible for the observed phenomenon and that the signal is also sensitive to the extent of reduction. Notably, because these defects influence the signal in the HAADF image as well as the LAADF image, it is possible that quantitative analysis of the intensity could be performed if a proper model were derived as input for the multislice routine [46,47].

Static displacements in general, whether due to vacancies or other phenomena, such as short-range chemical ordering, influence the scattering process and increase diffuse scattering for both electrons and X-rays [48,49]. The diffuse scattering generated by static displacements or other defects can be differentiated from the time-dependent thermally induced component due to phonon interactions (i.e., thermal diffuse scattering). This behavior can be described using the Patterson function and several situations have been considered [50]. In short, Bragg diffraction occurs from the periodic potential of a crystal while diffuse scattering will result from non-periodic components whether it arise from thermal motion or the presence of a defect. The presence of non-periodic components (defects) will decrease elastic Bragg scatter and

increase the diffuse background. The contribution of zero order Laue zone (ZOLZ) Bragg scattering to high angles and the HAADF signal is negligible. However, higher order Laue zones (HOLZ) reflections do contribute to the HAADF signal. These reflections are highly sensitive to disorder and will decrease in intensity with increasing lattice incoherency. The second mechanism that reduces intensity in the HAADF signal is related to electron channeling. Lattice distortions can significantly reduce channeling by virtue of the greater incoherency of the lattice [51]. This results in reduced high-angle scattering since the de-channeled electrons interact more weakly with the atomic nuclei [52,53]. In turn, lower angle scattering increases since the scattered electron intensity distribution more closely follows the distribution for kinematic scattering [54]. Due to the interplay of these scattering mechanisms, an increase in the LAADF and a decrease in the HAADF signal explains our experimental observations and those reported elsewhere [26,28]. It is worth noting that, in these previous reports, strain fields and displacements were generated at line defects or interfaces: in this report it is static displacements due to a chemical expansion, as a result of the oxygen vacancies, that has been shown to increase the LAADF signal while simultaneously reducing the HAADF signal.

Preliminary studies on MgO and $SrTiO_3$ suggest this technique can be expanded to other material systems. In Figs. 6 and 7, MgO and $SrTiO_3$ cubes, respectively, both orientated along $<100>$ directions and predominately terminated by {100} surfaces, also show enhancement of the LAADF signal near particle edges with a corresponding decrease in the HAADF signal (or approximately uniform in the MAADF signal). Furthermore, it is interesting to note that the length scale of the signal enhancement varies between samples. In the $SrTiO_3$ cube, the LAADF intensity increase is limited to approximately the first nanometer of the crystal surface, whereas, in the MgO cube, weak features can be seen extending into the crystal more than ≈ 8 nm from the surface. Bear in mind that LAADF-STEM is sensitive to *diffraction-based phenomena and distortions of the lattice* therefore it is prudent to verify the physical origin of the increased scattering to low angles. For example, a hydroxide phase, $Mg(OH)_2$, can readily form upon exposure to H_2O and it is possible the existence of a secondary hydroxide phase could be responsible for the observed contrast in Fig. 6a. This uncertainty emphasizes the need to employ an independent technique to pinpoint the origin of the observed contrast. The use of a spectroscopic technique such as EELS could be used to initially establish the physical origin of the signal enhancement prior to LAADF imaging, which could then be used to more easily track the phenomenon with a less rigorous experimental setup.

The origin of the intensity variations in the LAADF and HAADF images is due to the influence of lattice distortions on the electron channeling and scattering processes. Because this is a rather general phenomenon, this technique can be applicable to many other material systems, assuming that certain conditions are met. First, the material must be oriented to a low-order zone axis or conditions where strong channeling of the electron beam occurs (e.g., two-beam condition). Next, the process that is being tracked must introduce a lattice distortion that is sufficient to disrupt channeling and increase scattering to low angles to generate detectable contrast in the ADF images. Lastly, other phenomena that can contribute to the ADF signals should remain static or contribute only a small fraction of the variable signal; otherwise the interpretation will become convoluted. Therefore, the technique is not limited solely to tracking the reduction of ceria, but could be used to analyze other materials and other processes that introduce lattice strains and thereby influence the local electron-scattering behavior. For example, it may be possible to track the extent of surface nitriding or carburizing processes. Moreover, due to the relative ease of this approach it can be readily extended to *in situ* studies. In such dynamic scenarios, STEM-EELS may prove difficult to implement due to increased specimen drift or because the chemical processes being observed are transient as a function of temperature or gas environment.

4. Conclusions

LAADF STEM imaging is sensitive to the oxidation state of cerium ions in ceria nanoparticles. The contrast in the STEM ADF images is generated by the localized lattice disorder due to the change in ionic radius of cerium as it is reduced from Ce^{4+} to Ce^{3+}. These lattice distortions increase scattering to low angles and subsequently disrupt the electron channeling process and reduce the scattering to high angles and the signal in HAADF images. This technique provides a facile method to qualitatively identify the cerium oxidation state even at high-spatial resolution; this can supplant STEM-EELS spectrum imaging whose experimental implementation is significantly more taxing and can require more advanced (expensive) instrumentation. Because this image contrast is fundamentally based on electron channeling and disruptions caused by lattice distortions, this technique may be expanded beyond ceria and prove useful in the characterization of other materials that are also experiencing processes where strain or static displacements occur.

Acknowledgments

A portion of this research was performed while A.C.J.-P. held a National Research Council Research Associateship Award at the National Institute of Standards and Technology. W.D.W., A.D.R., J. S.D., K.Q., and B.C.S. thank the NSF for support under Grant DMR-1352328-CAREER, CHE-1308644, and the CCI Center for Nanostructured Electronic Materials (CHE-1038015). A.D.R. specifically acknowledges the University of Florida Howard Hughes Medical Institute Intramural Award. A portion of the work was carried out at the Center for Functional Nanomaterials at Brookhaven National Laboratory (Upton, NY) through User Proposal BNL-CFN-31913 and BNL-CFN-33789, supported by the U.S. Department of Energy (DOE), Office of Basic Energy Sciences, under Contract DE-SC0012704.

Disclaimer: Certain commercial equipment and materials are identified in this paper in order to specify adequately the experimental procedure. In no case does such identification imply recommendations by the National Institute of Standards and Technology nor does it imply that the material or equipment identified is necessarily the best available for this purpose.

Appendix A. Supplementary material

Supplementary data associated with this article can be found in the online version at http://dx.doi.org/10.1016/j.ultramic.2015.12.004.

References

[1] C. Sun, H. Li, L. Chen, Nanostructured ceria-based materials: synthesis, properties, and applications, Energy Environ. Sci. 5 (2012) 8475–8505.
[2] T. Manoubi, C. Colliex, P. Rez, Quantitative electron energy loss spectroscopy on M_{45} edges in rare earth oxides, J. Electron Spectrosc. Relat. Phenom. 50 (1990) 1–18.
[3] R. Sharma, P.A. Crozier, Z.C. Kang, L. Eyring, Observation of dynamic nanostructural and nanochemical changes in ceria-based catalysts during in-situ reduction, Philos. Mag. 84 (2007) 2731–2747.
[4] J.A. Mundy, Q. Mao, C.M. Brooks, D.G. Schlom, D.A. Muller, Atomic-resolution chemical imaging of oxygen local bonding environments by electron energy

loss spectroscopy, Appl. Phys. Lett. 101 (2012) 042907.
[5] D.A. Muller, L.F. Kourkoutis, M. Murfitt, J.H. Song, H.Y. Hwang, J. Silcox, N. Dellby, O.L. Krivanek, Atomic-scale chemical imaging of composition and bonding by aberration-corrected microscopy, Science 319 (2008) 1073–1076.
[6] D.A. Muller, Structure and bonding at the atomic scale by scanning transmission electron microscopy, Nat. Mater. 8 (2009) 263–270.
[7] H. Tan, S. Turner, E. Yücelen, J. Verbeeck, G. Van Tendeloo, 2D atomic mapping of oxidation states in transition metal oxides by scanning transmission electron microscopy and electron energy-loss spectroscopy, Phys. Rev. Lett. 107 (2011) 107602.
[8] S. Turner, S. Lazar, B. Freitag, R. Egoavil, J. Verbeeck, S. Put, Y. Strauven, G. Van Tendeloo, High resolution mapping of surface reduction in ceria nanoparticles, Nanoscale 3 (2011) 3385–3390.
[9] A. Gubbens, M. Barfels, C. Trevor, R. Twesten, P. Mooney, P. Thomas, N. Menon, B. Kraus, C. Mao, B. McGinn, The GIF Quantum, a next generation post-column imaging energy filter, Ultramicroscopy 110 (2010) 962–970.
[10] H.A. Brink, M.M.G. Barfels, R.P. Burgner, B.N. Edwards, A sub-50 meV spectrometer and energy filter for use in combination with 200 kV monochromated (S)TEMs, Ultramicroscopy 96 (2003) 367–384.
[11] M.P. Oxley, M. Varela, T.J. Pennycook, K. van Benthem, S.D. Findlay, A. J. D'Alfonso, L.J. Allen, S.J. Pennycook, Interpreting atomic-resolution spectroscopic images, Phys. Rev. B 76 (2007) 064303.
[12] S.D. Findlay, M.P. Oxley, L.J. Allen, Volcano structure in atomic resolution core-loss images, Ultramicroscopy 108 (2008) 677–687.
[13] R.F. Egerton, New techniques in electron energy-loss spectroscopy and energy-filtered imaging, Micron 34 (2003) 127–139.
[14] R.F. Egerton, Limits to the spatial, energy and momentum resolution of electron energy-loss spectroscopy, Ultramicroscopy 107 (2007) 575–586.
[15] P. Ercius, M. Boese, T. Duden, U. Dahmen, Operation of TEAM I in a user environment at NCEM, Microsc. Microanal. 18 (2012) 676–683.
[16] S.R. Gilliss, J. Bentley, C.B. Carter, Electron energy-loss spectroscopic study of the surface of ceria abrasives, Appl. Surf. Sci. 241 (2005) 61–67.
[17] L.A.J. Garvie, P.R. Buseck, Determination of Ce^{4+}/Ce^{3+} in electron-beam-damaged CeO_2 by electron energy-loss spectroscopy,, J. Phys. Chem. Solids 60 (1999) 1943–1947.
[18] S.J. Haigh, N.P. Young, H. Sawada, K. Takayanagi, A.I. Kirkland, Imaging the active surfaces of cerium dioxide nanoparticles, ChemPhysChem 12 (2011) 2397–2399.
[19] F. Zhang, P. Wang, J. Koberstein, S. Khalid, S.-W. Chan, Cerium oxidation state in ceria nanoparticles studied with X-ray photoelectron spectroscopy and absorption near edge spectroscopy, Surf. Sci. 563 (2004) 74–82.
[20] E. Paparazzo, XPS studies of damage induced by X-ray irradiation on CeO_2 surfaces, Surf. Sci. 234 (1990) L253–L258.
[21] M.N. Revoy, R.W.J. Scott, A.P. Grosvenor, Ceria nanocubes: dependence of the electronic structure on synthetic and experimental conditions, J. Phys. Chem. C. 117 (2013) 10095–10105.
[22] G.A. Botton, S. Lazar, C. Dwyer, Elemental mapping at the atomic scale using low accelerating voltages, Ultramicroscopy 110 (2010) 926–934.
[23] Z.L. Wang, Thermal diffuse scattering in sub-angstrom quantitative electron microscopy—phenomenon, effects and approaches, Micron 34 (2003) 141–155.
[24] D.D. Perovic, C.J. Rossouw, A. Howie, Imaging elastic strains in high-angle annular dark field scanning transmission electron microscopy, Ultramicroscopy 52 (1993) 353–359.
[25] L. Fitting, S. Thiel, A. Schmehl, J. Mannhart, D.A. Muller, Subtleties in ADF imaging and spatially resolved EELS: a case study of low-angle twist boundaries in $SrTiO_3$, Ultramicroscopy 106 (2006) 1053–1061.
[26] Z. Yu, D.A. Muller, J. Silcox, Study of strain fields at a-Si/c-Si interface, J. Appl. Phys. 95 (2004) 3362–3371.
[27] G. Duscher, S.J. Pennycook, N.D. Browning, R. Rupangudi, C. Takoudis, H.-J. Gao, R. Singh, Structure, composition and strain profiling of Si/SiO_2 interfaces, AIP Conf. Proc. 449 (1998) 191–195.
[28] P.J. Phillips, M. De Graef, L. Kovarik, A. Agrawal, W. Windl, M.J. Mills, Atomic-resolution defect contrast in low angle annular dark-field STEM, Ultramicroscopy 116 (2012) 47–55.
[29] V. Grillo, F. Rossi, A new insight on crystalline strain and defect features by STEM–ADF imaging, J. Cryst. Growth 318 (2011) 1151–1156.
[30] D.A. Muller, N. Nakagawa, A. Ohtomo, J.L. Grazul, H.Y. Hwang, Atomic-scale imaging of nanoengineered oxygen vacancy profiles in $SrTiO_3$, Nature 430 (2004) 657–661.
[31] Z. Wu, M. Li, D.R. Mullins, S.H. Overbury, Probing the surface sites of CeO_2 nanocrystals with well-defined surface planes via methanol adsorption and desorption, ACS Catal. 2 (2012) 2224–2234.
[32] L. Torrente-Murciano, A. Gilbank, B. Puertolas, T. Garcia, B. Solsona, D. Chadwick, Shape-dependency activity of nanostructured CeO_2 in the total oxidation of polycyclic aromatic hydrocarbons, Appl. Catal. B: Environ. 132–133 (2013) 116–122.
[33] F.A. Rabuffetti, H.-S. Kim, J.A. Enterkin, Y. Wang, C.H. Lanier, L.D. Marks, K. R. Poeppelmeier, P.C. Stair, Synthesis-dependent first-order Raman scattering in $SrTiO_3$ nanocubes at room temperature, Chem. Mater. 20 (2008) 5628–5635.
[34] I.S. Altman, I.E. Agranovski, M. Choi, On nanoparticle surface growth: MgO nanoparticle formation during a Mg particle combustion, Appl. Phys. Lett. 84 (2004) 5130–5132.
[35] J.M. LeBeau, S. Stemmer, Experimental quantification of annular dark-field images in scanning transmission electron microscopy, Ultramicroscopy 108 (2008) 1653–1658.
[36] M.M.J. Treacy, J.M. Gibson, Coherence and multiple scattering in "Z-contrast" images, Ultramicroscopy 52 (1993) 31–53.
[37] D.E. Jesson, S.J. Pennycook, Incoherent imaging of thin specimens using coherently scattered electrons, Proc. R. Soc. Lond. Ser. A: Math. Phys. Sci. 441 (1993) 261–281.
[38] P. Hartel, H. Rose, C. Dinges, Conditions and reasons for incoherent imaging in STEM, Ultramicroscopy 63 (1996) 93–114.
[39] Y. Lin, Z. Wu, J. Wen, K.R. Poeppelmeier, L.D. Marks, Imaging the atomic surface structures of CeO_2 nanoparticles, Nano Lett. 14 (2014) 191–196.
[40] H.W. Chiang, R.N. Blumenthal, R.A. Fournelle, A high-temperature lattice-parameter and dilatometer study of the defect structure of nonstoichiometric cerium dioxide, Solid State Ion. 66 (1993) 85–95.
[41] M. Mogensen, N.M. Sammes, G.A. Tompsett, Physical, chemical and electrochemical properties of pure and doped ceria, Solid State Ion. 129 (2000) 63–94.
[42] R. Shannon, Revised effective ionic radii and systematic studies of interatomic distances in halides and chalcogenides, Acta Crystallogr. Sect. A 32 (1976) 751–767.
[43] D. Marrocchelli, S.R. Bishop, H.L. Tuller, B. Yildiz, Understanding chemical expansion in non-stoichiometric oxides: ceria and zirconia case studies, Adv. Funct. Mater. 22 (2012) 1958–1965.
[44] C. Koch, Determination of Core Structure Periodicity and Point Defect Density Along Dislocations, Department of Physics, Arizona State University, Tempe AZ, 2002.
[45] M. Yashima, D. Ishimura, Y. Yamaguchi, K. Ohoyama, K. Kawachi, High-temperature neutron powder diffraction study of cerium dioxide CeO_2 up to 1770 K, Chem. Phys. Lett. 372 (2003) 784–787.
[46] T. Grieb, K. Muller, R. Fritz, M. Schowalter, N. Neugebohrn, N. Knaub, K. Volz, A. Rosenauer, Determination of the chemical composition of GaNAs using STEM HAADF imaging and STEM strain state analysis, Ultramicroscopy 117 (2012) 15–23.
[47] T. Grieb, K. Muller, R. Fritz, V. Grillo, M. Schowalter, K. Volz, A. Rosenauer, Quantitative chemical evaluation of dilute GaNAs using ADF STEM: avoiding surface strain induced artifacts, Ultramicroscopy 129 (2013) 1–9.
[48] K. Huang, X-ray reflexions from dilute solid solutions, Proc. R. Soc. Lond. Ser. A. Math. Phys. Sci. 190 (1947) 102–117.
[49] C.R. Hall, P.B. Hirsch, G.R. Booker, The effect of point defects on absorption of high energy electrons passing through crystals, Philos. Mag. 14 (1966) 979–989.
[50] J.M. Cowley, Diffraction Physics, Third ed., Elsevier, Amsterdam, 1995.
[51] T. Plamann, M.J. Hytch, Tests on the validity of the atomic column approximation for STEM probe propagation, Ultramicroscopy 78 (1999) 153–161.
[52] V. Grillo, E. Carlino, F. Glas, Influence of the static atomic displacement on atomic resolution Z-contrast imaging, Phys. Rev. B 77 (2008) 054103.
[53] V. Grillo, K. Mueller, K. Volz, F. Glas, T. Grieb, A. Rosenauer, Strain, composition and disorder in ADF imaging of semiconductors, J. Phys.: Conf. Ser. 326 (2011) 012006.
[54] J.M. Cowley, Y. Huang, De-channelling contrast in annular dark-field STEM, Ultramicroscopy 40 (1992) 171–180.